Linear and non-linear methods to analyse the drivability of a through-the-road parallel hybrid electric vehicle

Thomas Holdstock, Aldo Sorniotti*, Suryanto and Leo Shead

University of Surrey,
Guildford, Surrey, GU2 7XH, UK
E-mail: t.holdstock@surrey.ac.uk
E-mail: a.sorniotti@surrey.ac.uk
E-mail: zs00025@surrey.ac.uk
E-mail: leo.shead@intelligent-energy.com
*Corresponding author

Fabio Viotto, Carlo Cavallino and Stefano Bertolotto

Oerlikon Graziano SpA,
Via Cumiana 14, 10098 Rivoli (Torino), Italy
E-mail: fabio.viotto@oerlikon.com
E-mail: carlo.cavallino@oerlikon.com
E-mail: stefano.bertolotto@oerlikon.com

Abstract: This paper deals with the simulation of the low frequency drivability of through-the-road parallel (TTRP) hybrid electric vehicles (HEVs). The current literature relating to HEVs is predominantly focused on energy efficiency optimisation. However, the drivability of this HEV typology can be particularly critical, due to the interaction of the front and rear axle dynamics. The article presents an experimentally validated non-linear model of a TTRP HEV, consisting of a front axle driven by an internal combustion engine (ICE) with a six-speed transmission, and a rear axle powered by an electric motor with a prototype two-speed transmission. The simulated TTRP HEV is then considered with both driven axles, and drivability manoeuvres in conditions of constant gear are carried out. The results are analysed to study acceleration and jerk profiles, and understand the anti-jerk control system fundamentals through linearisation methods.

Keywords: through-the-road; parallel; hybrid; electric; drivability; simulation; control; linear; non-linear; vehicle.

Biographical notes: Thomas Holdstock received his BEng in Aerospace Engineering from the University of Surrey, UK, in 2007. After two years working in industry for a control systems company, he is currently studying for his PhD at the University of Surrey. His research focuses on the modelling and optimisation of state-of-the-art transmissions for electric vehicles, along with hardware-in-the-loop testing.

Aldo Sorniotti received his MSc in Mechanical Engineering and his PhD in Applied Mechanics from Politecnico di Torino, Italy, in 2001 and 2005, respectively. He is a Senior Lecturer in Advanced Vehicle Engineering at the University of Surrey, UK. His research interests focus on vehicle dynamics control and mechanical transmissions for fully electric and hybrid electric vehicles. He has authored over 80 conference and journal papers.

Suryanto received his MSc in Manufacturing from the University of Huddersfield, UK, in 1994. He was a Lecturer at the State Polytechnic of Ujung-Pandang, Indonesia. He is currently studying for his PhD at the University of Surrey, UK, working on the modelling and optimisation of hybrid electric vehicles.

Leo Shead completed his MEng in Mechanical Engineering at the University of Durham, UK, in 1999 and his PhD in Model Predictive Control Theory from the University of Sheffield in 2009. He worked on Hybrid Electric Vehicle Research at QinetiQ PLC (2000–2005), and as a Lecturer in Advanced Vehicle Systems Engineering at the University of Surrey, UK (2009–2012). He is now developing control systems for fuel cells at Intelligent Energy, Loughborough, UK.

Fabio Viotto received his MSc in Automotive Engineering from Politecnico di Torino, Italy, in 1998. He is a Product Manager for electric vehicle and hybrid electric vehicle applications in the Automotive Product Development Department at Oerlikon Graziano SpA, Italy. His research focus includes design and testing of electric and hybrid electric vehicle drivetrains. He has actively cooperated in writing several technical papers.

Carlo Cavallino received his MSc in Mechanical Engineering from Politecnico di Torino, Italy, in 2004. He is a Project Development Engineer at Oerlikon Graziano SpA, Italy. His professional and research interests include design and testing of dual clutch and automated manual transmission systems for automotive applications. He has actively cooperated in writing several technical papers about the subject.

Stefano Bertolotto received his MSc in Automotive Engineering from Politecnico di Torino, Italy, in 2010. He is a Design Engineer at Oerlikon Graziano, SpA, Italy, working on the development and testing of mechanical transmissions for electric and hybrid electric vehicles and has authored several technical papers about the subject.

1 Introduction

Drivability is an important factor that needs to be considered when developing the drivetrain, internal combustion engine (ICE) or electric motor control, gearshift control, suspension system and powertrain mounting system of any vehicle. The low frequency

drivability of a vehicle is generally measured through acceleration and jerk (rate of acceleration) profiles during set manoeuvres such as acceleration and tip-in tests (Dorey and Holmes, 1999; Sorniotti, 2008), with a magnitude of jerk over $10m/s^3$ being considered unacceptable according to some sources (Huang and Wang, 2004). Some authors also consider the frequency of the jerk oscillations and the root mean square (RMS) jerk, stating that a value of jerk up to about 25 m/s^3 can be tolerated for frequencies less than 3 Hz (Shouren, 1984).

A conventional parallel hybrid electric vehicle (HEV) layout consists of an ICE and an electric motor placed on the same axle with the torque of each power source driving the same wheels (Arata et al., 2011). A significant body of literature has been published concerning the control of the mode transitions and gearshifts within parallel HEVs (e.g., Gupta et al., 2009; Shin et al., 2010). Kim et al. (2009) explain that the HEV drivability can be improved through controlling the clutch slip.

The drivability in conditions of constant gear is particularly relevant when considering a through-the-road parallel (TTRP) HEV as two power sources (one for each axle), each with different steady-state and dynamic characteristics, are both simultaneously providing torque, and are coupled to transmission systems with different parameters (gear ratios, inertias and torsion stiffness). In a TTRP HEV, each axle is driven, and thus the vehicle is all-wheel-drive (AWD), consequently benefitting from increased traction capabilities. A HEV in this configuration can work in three modes: front-wheel-drive (FWD) driven by the ICE in the case study vehicle, rear-wheel-drive (RWD) driven by the electric motor (centrally located and connected to the wheels through half-shafts in the case study vehicle), and AWD driven by both axles in a parallel layout. This arrangement allows each driving mode to be adopted for specific driving conditions and the electric motor to be utilised to reduce the ICE fuel consumption through the improvement of the location of the ICE operating points and the implementation of brake regeneration. Moreover, the electric motor improves vehicle performance and/or allows the ICE to be downsized. The work of Sorniotti et al. (2011) deals with the seamless gearshift control of an electric axle for fully electric vehicles or TTRP HEVs.

As the ICE and electric motor have different torque and power curves and efficiency maps, the operating points need to be carefully controlled. The ideal electric motor torque characteristic (as a function of motor speed) is theoretically very favourable from the viewpoint of vehicle response, due to the constant torque achievable at low motor speeds, going into a constant power region for high values of electric motor speed. Furthermore, the lack of combustion and consequent torque fluctuations typical of ICEs forego the need of a clutch damper. However, the lack of the clutch damper eliminates the main damping component within the transmission, and can give rise to non-optimal drivability, especially if there are significant plays within the transmission system (Amann et al., 2004). In addition, the ease of control and typically low reaction time of electric motor drives allow an effective implementation of anti-jerk and motor torque control algorithms to reduce driveline oscillations. The potentially low reaction time of the electric motor drive also improves the driver's subjective rating of vehicle responsiveness when an abrupt driver torque demand is applied, but can also excite undesired drivetrain oscillations.

Several articles have presented anti-jerk controllers for ICE-driven powertrains, in order to reduce vehicle jerk and driveline oscillations. A typical anti-jerk controller adopted by vehicle manufacturers, including its tuning procedure, is described by

Schöggl et al. (2002). The control approach is very basic and empirical; however it guarantees the required robustness for an industrial application of the controller. Academic researchers have developed anti-jerk controllers with a more sophisticated control structure, potentially giving better results. An example of a more advanced anti-jerk control system for a FWD ICE driven vehicle utilises a neuro-fuzzy approach (Torkzadeh et al., 2003), to control the requested torque. A second example of an anti-jerk control system for a FWD vehicle is based on a state-space model to provide a robust controller which is capable of adapting the control either for component wear or for a specific drivetrain mechanical design (Baumann et al., 2005).

Very few studies deal with electric axle drivability (e.g., Amann et al., 2004; Bottiglione et al., 2012). They are predominantly based on feedback control algorithms for the compensation of low frequency drivetrain oscillations, where driveshaft torque is estimated through non-linear observers. A study (Fredriksson, 2006) has shown that a drivability control system for a parallel HEV (but not TTRP HEV) can be implemented through controlling the electric motor and ICE to dampen the driveline oscillations.

The previously referenced drivability analysis studies focused on ICE drivetrains, fully-electric vehicles and parallel HEVs. The research presented in this paper will focus on the drivability analysis of TTRP HEVs, particularly on the dynamic interaction between the two powertrains. Moreover, the development of a model-based anti-jerk control system will be outlined. A non-linear modelling method has been adopted due to the need to consider the characteristics of the clutch damper, tyres and vehicle suspension system in the time domain (Sorniotti, 2008). A linear model can be developed to understand the frequency response of the vehicle and for fixed gear tip-in tests, which generally excite oscillations at the first natural frequency of each axle, in the 2-10 Hz range (Morina, 2010). An anti-jerk controller can be designed using the linear model. However, for realistic analysis in the time domain, a non-linear model is required.

For a TTRP, the hardware components of the ICE and electric powertrains are usually designed separately (often by different companies) and constitute two completely independent subsystems (this characteristic differentiates a TTRP HEV from a common parallel HEV). Therefore, the article will present the description and the validation of the models of the two powertrains, and then it will deal with their dynamic interaction, which constitutes the main contribution of the research as this has been done in the past for parallel HEVs, but only state transitions have been researched for TTRP HEVs. Finally, the development of an anti-jerk controller for the overall system will be outlined.

2 Non-linear drivetrain and vehicle model

Non-linear powertrain models have been developed to simulate each separate drivetrain component of the TTRP HEV, along with a non-linear vehicle chassis model to analyse vehicle motion and pitch dynamics. The overall model is characterised by 16 degrees of freedom, nine of which are depicted in Figure 1 (front axle: engine rotation, rotation of transmission from primary shaft to gearbox differential case, relative rotation between the two sun gears of the differential, two wheel rotations. Rear axle: rotation of the electric powertrain from the motor to the differential casing, relative rotation between the two sun gears, two wheel rotations), which is the vehicle powertrain schematic.

Figure 1   Schematic of the TTRP HEV powertrain
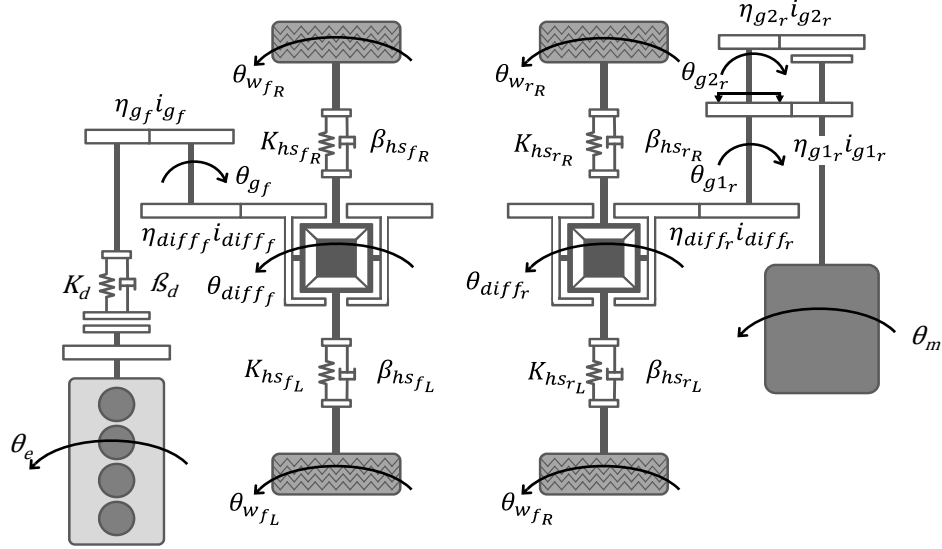
2.1   *Internal-combustion-engine-driven front axle*

The ICE drivetrain model (from the engine to the half-shaft) has two degrees of freedom due to the non-linear torsional dynamics of the clutch damper. An additional degree of freedom can be represented by the internal dynamics of the differential gearset, which gives rise to a different angular speed on the left and right sun gears. This is relevant only in case of uneven friction coefficients on the two tyres of the same axle, or asymmetric half-shafts.

The engine is modelled through experimentally attained maps (torque characteristic and specific fuel consumption), which generate a theoretical engine torque $T_{e_{theor}}$. Each component has been modelled considering its experimentally derived efficiency map expressed as a function of the operating torque, angular speed, operating temperature and gear ratio (where applicable). Additional data, including gear ratios, inertias, half-shaft stiffness/damping values, etc., for the ICE axle model were provided by the industrial partners to match the test vehicle adopted for the validation of the ICE drivetrain model. The engine dynamics are described through a first order transfer function that depends on the engine characteristics and must be carefully tuned especially in the case of a turbo-charged unit. The output of the transfer function is the delayed torque $T_{e_{del}}$ that is used for the moment balance equation of the engine shaft:

$$T_{e_{del}} - T_{cd} = J_e \ddot{\theta}_e \tag{2.1}$$

The clutch damper model includes the typical non-linear torque characteristic as a function of its torsion angle, due to the elastic properties of its springs and the geometry of the component. Also the variation of the degree of clutch damper hysteresis as a function of its torsion angle is modelled, which depends on the level of Coulomb friction within the component. Marginal modifications to the model can be implemented for a

case study vehicle utilising a dual mass flywheel. The moment balance equation for the whole transmission from the clutch damper to the differential is given by:

$$T_{cd}i_{g_f}\eta_{g_f}i_{dif_f}\eta_{diff_f} - \left(\frac{T_{hs_{f_R}} + \frac{1}{2}J_{hs_{f_R}}\ddot{\theta}_{diff_{f_R}}}{\eta_{CVin_{f_R}}} + \frac{T_{hs_{f_L}} + \frac{1}{2}J_{hs_{f_L}}\ddot{\theta}_{diff_{f_L}}}{\eta_{CVin_{f_L}}} \right) = J_{trans_{ICE}}\ddot{\theta}_{diff_f} \quad (2.2)$$

where the equivalent moment of inertia, $J_{trans_{ICE}}$, is:

$$J_{trans_{ICE}} = J_{g1_f}i_{g_f}^2\eta_{g_f}i_{diff_f}^2\eta_{diff_f} + J_{g2_f}^2i_{diff_f}^2\eta_{diff_f} + J_{diff_f} \quad (2.3)$$

The efficiencies of the different components can be reciprocated in the formulas depending on the sign of their input torque. The efficiencies of the constant velocity joints are relevant for a case where there is significant inclination of the half-shafts, induced by the relative motions of the sprung and unsprung masses. Therefore, they can be represented by a look-up-table depending on the inclination angle. The internal dynamics of the differential gearset is modelled by:

$$\frac{T_{hs_{f_R}} + \frac{1}{2}J_{hs_{f_R}}\ddot{\theta}_{diff_{f_R}}}{\eta_{CVin_{f_R}}} - \frac{T_{hs_{f_L}} + \frac{1}{2}J_{hs_{f_L}}\ddot{\theta}_{diff_{f_L}}}{\eta_{CVin_{f_L}}} = J_{diff_{mech}}\Delta\ddot{\theta}_{diff_f} \quad (2.4)$$

The half-shafts are modelled as a spring and damper (representing the internal damping of the material, steel in this case) system, which simulates the torsional dynamics through considering a separate mass moment of inertia at the wheel and differential end.

The tyre longitudinal force is modelled by using the well known Pacejka Magic Formula (Pacejka, 2006), which calculates the longitudinal force as a function of the vertical tyre load, slip ratio and friction coefficient. The tyre model adopted in the paper includes a relaxation length model, based on a non-linear first order differential equation (because of the variation of the relaxation length depending on the operating conditions, mainly vertical load and slip ratio).

2.2 *Electric-motor-driven rear axle*

The rear axle consists of a permanent magnet electric motor and a novel two-speed prototype transmission developed by Oerlikon Graziano. The two-speed transmission employs a dual-stage spur-gear reduction. In order to change gear the transmission utilises a seamless shift system (Cavallino, 2009). The primary components of the shift system are a one-way sprag clutch and a friction clutch, transferring torque in first and second gear respectively as displayed in Figure 2.

The friction clutch is electro-hydraulically controlled through the use of a remote brushless-motor-driven actuator (Sorniotti et al., 2011). The engagement of a locking ring prevents the one-way sprag clutch from overrunning when the direction of torque through the transmission is reversed in order to allow regenerative energy recovery whilst decelerating in first gear. The sprag clutch is characterised by approximately two degrees of play (here neglected) and marginal torsional deformation during engagement.

Figure 2   Schematic of the gearbox operation in (a) first gear and (b) second gear (see online version for colours)

(a)   (b)
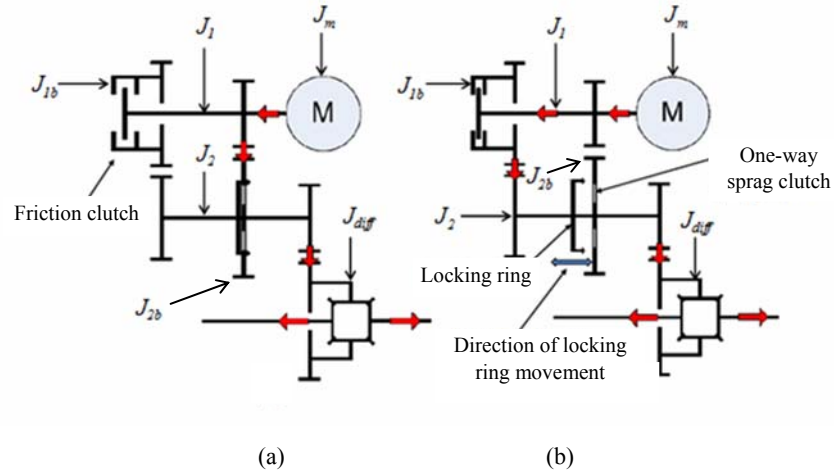
Because of the absence of a clutch damper, the rear axle is a one degree of freedom system in conditions of constant gear (two degrees of freedom when including the internal dynamics of the differential gearset) and as such there is only one moment balance equation governing the electric motor output to the differential case output.

The air gap torque $T_{m_{del}}$ of the electric motor drive is calculated through a first order transfer function, which receives a theoretical torque demand calculated by the energy management system originating from the accelerator pedal position and the drivetrain operating conditions. Also the slew rate and the windage torque of the electric motor drive are considered. The moment balance equations of the transmission shafts differ for each selected gear, therefore the derived differential accelerations in gear one and two are given below, in equations (2.5) and (2.7) respectively.

$$T_{m_{del}} i_{g1_r} \eta_{g1_r} i_{diff_r} \eta_{diff_r} + T_{fc} i_{g2_r} \eta_{g2_r} i_{diff_r} \eta_{diff_r} - T_{fc} i_{g1_r} \eta_{g1_r} i_{diff_r} \eta_{diff_r}$$
$$- \left(\frac{T_{hs_{fR}} + \frac{1}{2} J_{hs_{fR}} \ddot{\theta}_{diff_{fR}}}{\eta_{CVin_{fR}}} + \frac{T_{hs_{fL}} + \frac{1}{2} J_{hs_{fL}} \ddot{\theta}_{diff_{fL}}}{\eta_{CVin_{fL}}} \right) = J_{EM_1} \ddot{\theta}_{diff_r} \qquad (2.5)$$

where the equivalent moment of inertia of the electric drivetrain in first gear, J_{EM_1}, is:

$$J_{EM_1} = J_{diff_r} + \left(J_m + J_1 \right) i_{diff_r}^2 \eta_{diff_r} i_{g1_r}^2 \eta_{g1_r} + J_{1b} i_{diff_r}^2 \eta_{diff_r} i_{g2_r}^2 \eta_{g2_r}$$
$$+ \left(J_2 + J_{2b} \right) i_{diff_r}^2 \eta_{diff_r} \qquad (2.6)$$

$$T_{m_{del}} i_{g2_r} \eta_{g2_r} i_{diff_r} \eta_{diff_r} - \left(\frac{T_{hs_{fR}} + \frac{1}{2} J_{hs_{fR}} \ddot{\theta}_{diff_{fR}}}{\eta_{CVin_{fR}}} + \frac{T_{hs_{fL}} + \frac{1}{2} J_{hs_{fL}} \ddot{\theta}_{diff_{fL}}}{\eta_{CVin_{fL}}} \right) = J_{EM_2} \ddot{\theta}_{diff_r} \quad (2.7)$$

where the equivalent moment of inertia of the electric drivetrain in second gear, J_{EM_2}, is:

$$J_{EM_2} = J_{diff_r} + \left(J_m + J_1 + J_{1b}\right)i_{diff_r}^2 \eta_{diff_r} i_{g2_r}^2 \eta_{g2_r}$$
$$+ \frac{J_{2b}i_{diff_r}^2 \eta_{diff_r} i_{g2_r}^2 \eta_{g2_r}}{i_{1_r}^2 \eta_{g1_r}} + J_2 i_{diff_r}^2 \eta_{diff_r} \tag{2.8}$$

Also in this case the efficiencies can be reciprocated depending on the signs of the torques through the individual components. The differential and wheel-related equations are similar to those implemented for the engine-driven axle.

2.3 Vehicle model

The vehicle model includes the sprung mass (chassis and body, Figure 3) and the unsprung masses (wheels and suspension systems). A trailing arm configuration has been adopted for the suspension model, as any suspension design can be modelled using this layout, through a graphical equivalency procedure (Reimpell et al., 2000) starting either from the three-dimensional suspension geometry, or from the experimental characterisation of the suspension elasto-kinematics (i.e., wheel longitudinal displacement as a function of bump). The variation of the equivalent pivot point (represented by the dimensions *c* to *f* in Figure 3) of the trailing arm onto the chassis can be easily incorporated in the form of a look-up-table within the model. Therefore, this simplified but representative model includes the non-linear anti-dive, anti-lift and anti-squat characteristics of the suspension systems, which affect the sprung mass pitch dynamics.

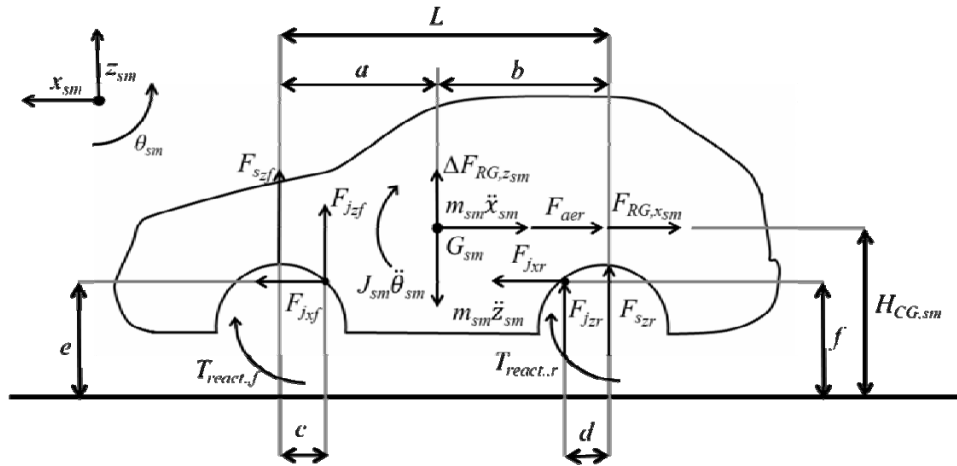**Figure 3**   Schematic of the vehicle sprung mass model

Figure 3 is the free body diagram of the vehicle sprung mass. The longitudinal acceleration of the vehicle is found from the sprung mass longitudinal force balance equation, equation (2.9). The tractive forces from the tyres are transmitted to the vehicle through the suspension joints; the external forces that affect the sprung mass are also

included, namely, the aerodynamic drag force and the unsprung mass force due to the road angle.

$$m_{sm}\ddot{x}_{sm} = \sum_{k=L,R} F_{j_{x_{f,k}}} + \sum_{k=L,R} F_{j_{x_{r,k}}} - F_{aer} - F_{RG,x_{sm}} \tag{2.9}$$

The sprung mass vertical force balance is shown in equation (2.10), giving the sprung mass vertical acceleration. This includes the vertical forces transmitted by the suspension arms through the suspension joints, the forces caused by the spring and damper system, along with the force induced by the road angle.

$$m_{sm}\ddot{z}_{sm} = \sum_{k=L,R} F_{j_{z_{f,k}}} + \sum_{k=L,R} F_{j_{z_{r,k}}} + \sum_{k=L,R} F_{s_{z_{f,k}}} + \sum_{k=L,R} F_{s_{z_{r,k}}} + \Delta F_{RG,z_{sm}} \tag{2.10}$$

The final degree of freedom, the sprung mass angular acceleration, or through integration, pitch, is found through considering the moment balance equation about the sprung mass centre of gravity and is shown in equation (2.11).

$$\begin{aligned} J_{sm}\ddot{\theta}_{sm} = & -\left(F_{s_{z_{f,R}}} + F_{s_{z_{f,L}}}\right)a - \left(F_{j_{z_{f,R}}} + F_{j_{z_{f,L}}}\right)(a-c) + \left(F_{s_{z_{r,R}}} + F_{s_{z_{r,L}}}\right)b \\ & + \left(F_{j_{z_{r,R}}} + F_{j_{z_{r,L}}}\right)(b-d) + \left(F_{j_{x_{f,R}}} + F_{j_{x_{f,L}}}\right)\left(H_{CG,sm} - e\right) \\ & + \left(F_{j_{x_{r,R}}} + F_{j_{x_{r,L}}}\right)\left(H_{CG,sm} - f\right) - T_{react.,f} - T_{react.,r} \end{aligned} \tag{2.11}$$

The spring and the damper forces are modelled through non-linear look-up-tables at the wheel centre. Therefore the model requires the relative vertical displacement and velocity between the unsprung and sprung mass as input data to calculate the equivalent suspension force.

Currently, the model presented neglects the dynamic effect of the mounting system of the two powertrains. This subject has been studied in Eller and Hetet (2010) and Sorniotti (2008), and requires further analysis, as the powertrain mounting system applies longitudinal and vertical forces to the chassis during torque transients, with a direct impact on vehicle drivability.

Figure 4   Schematic of the vehicle front unsprung mass

(a)   (b)
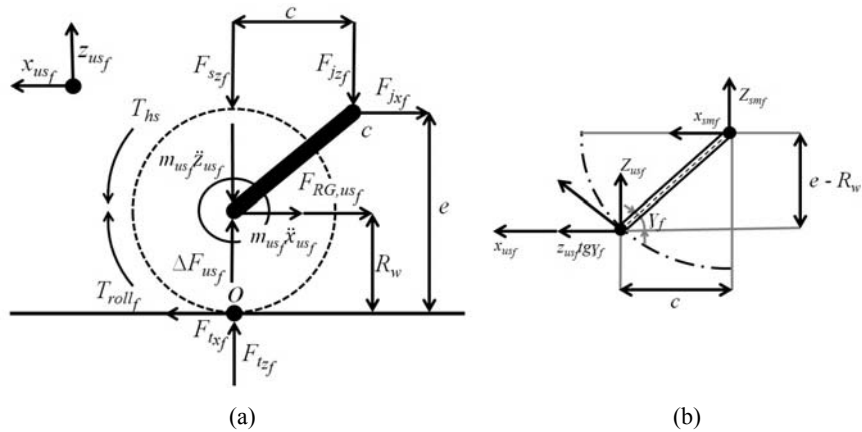
A schematic of the free body diagram of a front unsprung mass is shown in Figure 4(a), along with the equivalent diagram of the suspension arm, Figure 4(b). The unsprung mass equations are developed to ascertain the longitudinal, vertical and angular motions, which represent a single degree of freedom (as the three displacements are kinematically linked to each other), and the longitudinal, F_{j_x}, and vertical, F_{j_z}, forces at the pivot point of the suspension arm. The tyre vertical dynamics are modelled with a linear (or non-linear, depending on the data availability) spring and damper approach.

3 Experimental validation of the model

The model presented in Section 2 was developed within the design of the hardware components and control software of a TTRP HEV, which has not been physically implemented yet. Therefore, the front ICE-driven axle was validated against data from a FWD test vehicle, and the rear axle against results attained from the electric axle prototype (the layout is shown in Figure 2) installed on a hardware-in-the-loop (HIL) test rig at the University of Surrey.

3.1 Internal combustion engine driven axle

The test data for the ICE-driven vehicle have been collected from a FWD vehicle fitted with a drivetrain comprised of an ICE and a five-speed automated manual transmission. The ICE test vehicle parameters are in the Appendix. The test vehicle carried out tip-in tests in conditions of fixed gear with a starting speed ranging from 12 km/h for first gear to 45 km/h in fifth gear, in order to perform the manoeuvres at similar initial values of engine speed. During the initial part of a tip-in test the vehicle maintains a constant speed. This requires a torque demand, expressed as a percentage of the maximum engine torque, which has a value that is a function of the gear ratio and initial vehicle speed. Then the driver applies a throttle input at a set rate, ideally according to a step input. In practice, the actual torque applied by the driver is not a step input but has been recorded during the experimental tests. The results from the test vehicle are displayed in Figure 5, for tip-in tests in different gears, with a final condition of wide open throttle. The figure shows an oscillation in the acceleration profiles for each gear, with the average acceleration level for each gear reducing with gear number. Table 1 presents the natural frequency for each tip-in test along with the damping ratio calculated through two methods adopted for the identification of the properties of second order systems: exponential decay and percentage overshoot (OS) (Nise, 2004). The automated routine used to calculate the damping ratio for the exponential decay method minimises the sum of the absolute value of the errors for the first three peaks. The frequency (measured as the average of the frequency values of the first three oscillations following the tip-in) of the acceleration oscillations and their OS can be seen to increase with each gear number whilst the damping ratio decreases with gear number as shown in Table 1, which is typical behaviour for this kind of test. This is true for both identification methods, although with the exponential decay method the second gear damping ratio does not fit the first acceleration oscillation peak. Despite the fact that the overall qualitative shape of the characteristic of vehicle longitudinal acceleration response resembles a second order system, the response of the equivalent second order transfer function (not reported here)

is very different from the actual vehicle response, which fully justifies the adoption of more complex models, such as those presented in this article. This is also confirmed by the very different values of the damping ratios calculated through the two alternative methods.

Figure 5   Experimental acceleration profiles during tip-in tests (with a final condition of wide open throttle rapidly applied at about two seconds, the actual time scale of the experimental results has been shifted) for different transmission ratios
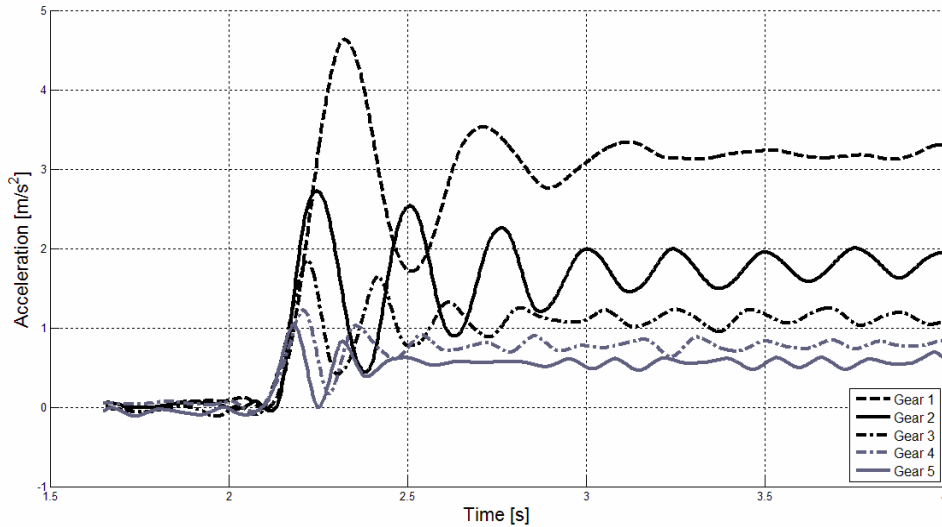

Table 1   Oscillation frequency, percentage overshoot and equivalent damping ratio of the longitudinal acceleration profile during experimental tip-in tests for different gears

	Gear I	Gear II	Gear III	Gear IV	Gear V
Natural frequency [Hz]	2.58	4.02	5.08	5.97	6.56
Overshoot [%]	30.90	29.26	35.12	36.89	47.18
Damping ratio $\zeta_{\%OS}$[-] (% OS)	0.35	0.36	0.32	0.30	0.23
Damping ratio ζ_{exp}[-] (exp. decay)	0.32	0.13	0.15	0.14	0.10

The TTRP HEV model was modified by removing the rear electric axle, and with it any torque input to the rear wheels, to have the same parameters as the real world test vehicle. The vehicle and transmission physical parameters have been directly inputted into the vehicle simulator, without any parameter fitting in order to match the experimental results. The results from the simulation model of Section 2 and the test data have been overlapped in Figure 6 for a first gear tip-in test, comparing the engine torque, vehicle speed, acceleration and jerk. The same torque demand profiles as the ones recorded during the experimental tests were adopted during the simulations. The figures show that the simulated results accurately follow the results of the test data, applying the correct amount of engine torque, and provoking the correct vehicle speed, acceleration and jerk response. A similar fit between the experimental and simulation results has been achieved for all the tip-in manoeuvres in the different gear ratios.

Figure 6 Experimental validation of the engine axle vehicle model on the test vehicle, first gear, initial speed of 12 km/h, final value of 100% throttle position
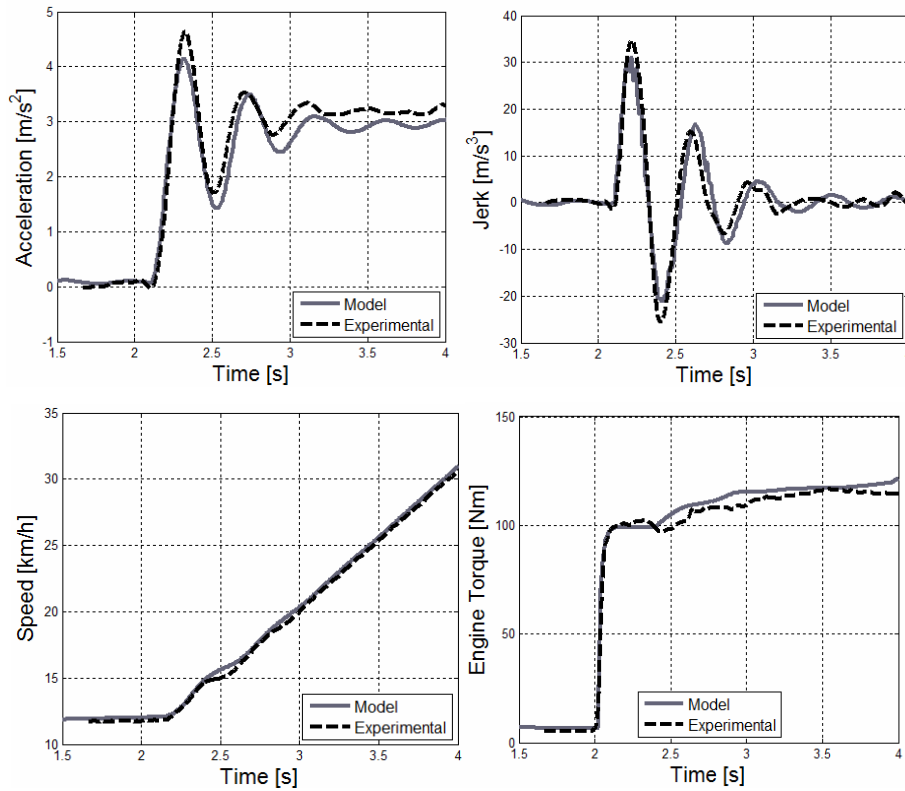
3.2 Electric-motor-driven axle

The rear axle of the TTRP HEV has been validated using a similar methodology to the front ICE-driven axle. The TTRP HEV model was adapted to only be driven by the rear axle, with the synchronisers of the ICE transmission open, removing any engine torque from the front wheels.

The rear electric motor drivetrain on the TTRP HEV considered in this paper is a prototype system and as such is not installed on a test vehicle at present. However, the drivetrain is installed on a HIL test rig (Figure 7) at the University of Surrey which allows driving manoeuvres to be carried out in real time. The test piece consists of the test electric motor drive, the prototype two-speed transmission (including the gearbox and the differential), the half-shafts and the wheel hubs. The rig consists of two induction motors which can provide a maximum hub torque of 1,925 Nm each and a peak power of 90 kW each. The system is controlled via a manoeuvre selector coupled to a dSpace unit which links to each component over controller area network (CAN) buses, a first bus for the communication between the rig and the vehicle model, and a second bus for the communication between the vehicle model and the testpiece (motor drive and transmission). The second CAN bus is identical to the CAN bus within the actual vehicle, in order to achieve a realistic emulation of the system delays. For this reason, the second

CAN bus has been kept separate from the first CAN bus, adopted for the management of the rig control. The second CAN bus must be altered to suit the test piece installed on the rig. The test electric motor drive is fed by a dedicated power supply which allows regenerative braking, whilst the hub motors are powered by separate power supplies fed from the grid. The vehicle model demands a torque from the test piece, whilst receiving a hub torque which is sent to the model to calculate the angular dynamics of the driven wheels and the longitudinal dynamics of the vehicle. The reference angular speed of each wheel is calculated by the vehicle model and is sent to the rig through the CAN interface, to simulate the correct vehicle response in real time.

The tip-in tests were simulated at varying initial speeds, 10 km/h, 30 km/h, 50 km/h and 70 km/h in both gears on both the model and the HIL test rig. An example of a test is shown in Figure 8, where the simulated results accurately overlap the experimental results. The vehicle model is identical for both the simulation and the model employed in the HIL test rig.

The electric motor adopted for the experimental tests is characterised by a relatively high moment of inertia and a significant time constant for the air gap torque generation, which reduces the jerk response of the system. Consequently, the higher motor rise time is beneficial from a drivability viewpoint, although this reduces the vehicle responsiveness. The authors have simulated motors with reduced time constants and found this parameter to have a considerable effect on the vehicle jerk, provoking significant oscillations of the longitudinal acceleration profile during tip-in tests, which indicates a requirement for an anti-jerk controller.

Figure 7   Schematic of the University of Surrey HIL electric axle rig (see online version for colours)
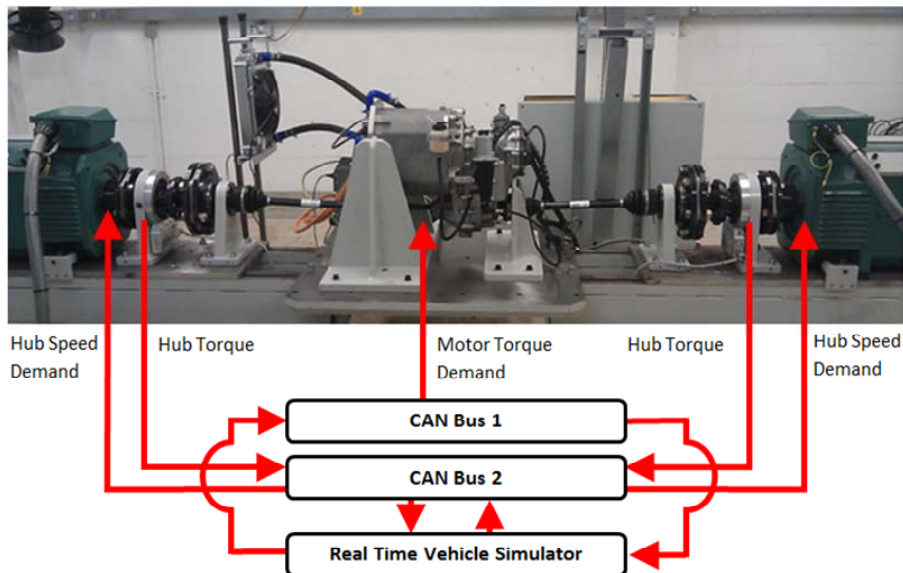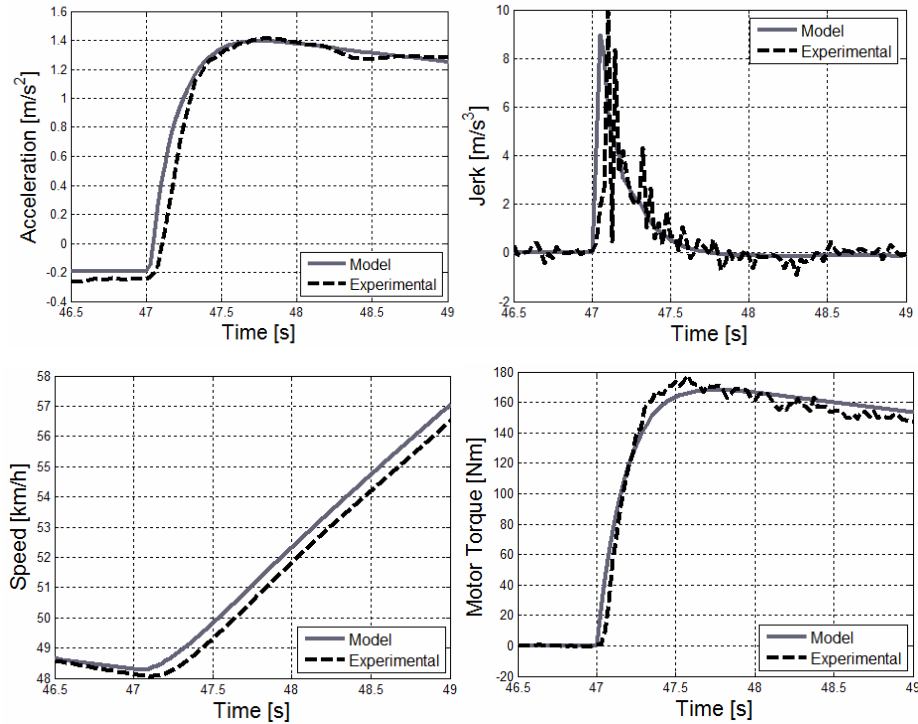
Figure 8 Experimental validation of the electric axle vehicle model on the HIL rig at the University of Surrey, initial speed of approximately 50 km/h, second gear

4 Analysis of the TTRP HEV drivability

The TTRP HEV model has been developed to analyse the effect of this powertrain layout on vehicle drivability during tip-in tests. Through proving the accuracy of each drivetrain model following the validation methods presented in Sections 3.1–3.2, the whole TTRP HEV model can be thought to be reliable and suitable for predictive analysis and anti-jerk control design. The main vehicle parameters of the case study adopted in this section are reported in the Appendix.

4.1 Sensitivity analysis

The drivability of the TTRP HEV has been analysed by simulating tip-in tests to consider the drivetrain response and vehicle acceleration in the time domain. In addition, a sensitivity analysis was carried out to research the effect of the torque distribution between the front and rear axles on the drivability, for the same overall value of wheel torque. In fact, depending on the energy efficiency maps of the two powertrains, driving mode, state of charge of the battery, the TTRP HEV supervisory controller (energy management system) can decide to split the torque demand between the two axles in a variety of possible distributions, provided that the torque demand is not so high as to require full torque from both powertrains. As a consequence, the average steady-state

vehicle acceleration will be the same for whatever torque split, however the jerk dynamics during the transient may be very different, depending on the torque distribution and the selected gear for each axle. In order to calculate the necessary torque demands to give the required wheel torque distribution and overall torque, the model initially computes the required steady-state values of the total front and rear wheel torques during a manoeuvre for the assigned accelerator pedal input. The model then backwards calculates the ICE and electric motor torque demands in steady-state conditions to provide the target wheel torque distribution level whilst retaining the required total steady-state wheel torque value during the manoeuvre.

The acceleration profiles of a tip-in test carried out at 27 km/h (initial speed), with the ICE transmission in third gear and with the rear transmission in first and second gear, are presented in Figures 9 and 10 respectively, for different wheel torque distributions. Both figures show an increase of the vehicle longitudinal acceleration oscillations for an increase of the engine driven axle torque. In particular, the electric axle of the specific vehicle application does not give rise to any significant oscillations during the second gear test, and low amplitude oscillations during the first gear test, whilst the engine-driven axle always produces significant oscillations. The experience of the authors of this contribution is that the electric axle results can significantly vary depending on the set of vehicle parameters. In particular the response time and the mass moment of inertia of the electric motor drive are different, for example, for permanent magnet and switched reluctance machines.

In Figures 9 and 10, the variety of the TTRP HEV responses for the same steady-state value of longitudinal acceleration level is very wide. The rear drivetrain wheel torque is lower when in second gear, which gives rise to lower acceleration values, as can be seen in Figure 10.

Figure 9   Sensitivity analysis of the front/rear axle torque distribution during a tip-in test at 27 km/h; front transmission: third gear, rear transmission: first gear
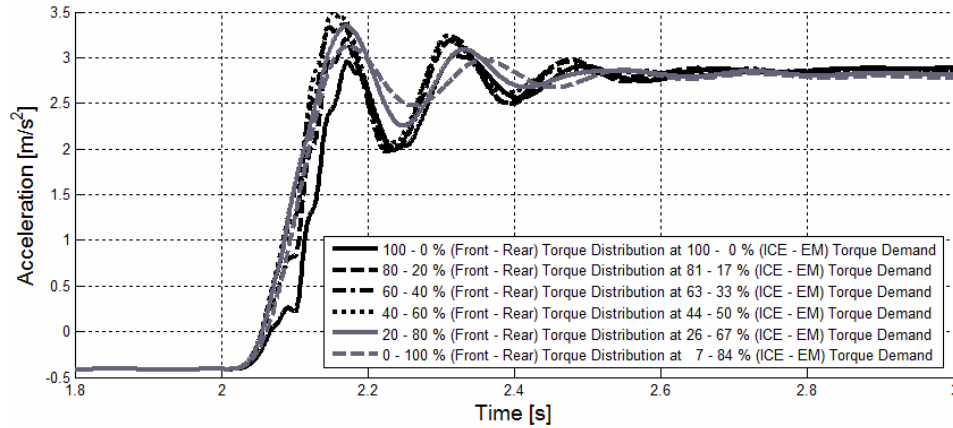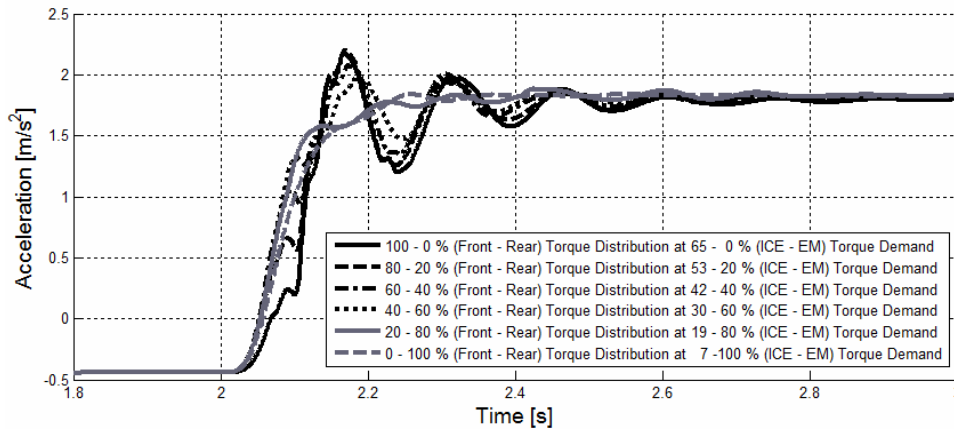
Figure 10 Sensitivity analysis of the front/rear axle torque distribution during a tip-in test at 27 km/h; front transmission: third gear, rear transmission: second gear

The response seen in Figures 9 and 10 is a function of the vehicle parameters. For example, in a parallel research activity based on the linear model of a TTRP HEV in the frequency domain, Morina (2010) has observed that the first natural frequencies of the two powertrains are very close to each other. In that case study vehicle, the resulting longitudinal acceleration response of the linear model in the time domain is characterised by the overlap of the under damped oscillations (with similar amplitudes and similar, but not identical, frequencies) caused by the two drivetrains, which gives rise to an irregular response, very different from the typical response of a conventional vehicle, shown in Figure 5, which, despite the potentially high levels of jerk, is characterised by a regular shape.

The speed profiles for two manoeuvres shown in Figure 10 are presented in Figures 11 and 12. The speeds of the different components, such as the engine and electric motor, are referred to the vehicle speed (i.e., the engine speed is divided by selected gear ratio and differential ratio and multiplied by the wheel radius). As a consequence, the figures allow the concurrent evaluation of the torsion dynamics of both powertrains during the test.

Figure 11 clearly shows the initial torsion of the clutch damper, before the first set of clutch springs starts to transmit the torque, and the subsequent internal dynamics of the component. Also, the difference between the differential speed and the front wheel speed (here the average value between the left and right wheel is considered) on the ICE-driven axle and the difference between the electric motor speed and the rear wheel speed on the electric-motor-driven axle are due to the half-shaft torsion dynamics. Each couple of speeds tends to converge at the end of the transient, when the half-shaft reaches the steady-state torsion angle for that value of transmitted torque. In both figures, the tyre slip ratio dynamics are evident from the difference between the vehicle speed and the respective wheel speed. At the conclusion of the transient, the wheel speed profile is higher on the axle transmitting the majority of the torque, the front one in Figure 11 and the rear one in Figure 12.

Figure 11   Speed comparison with each component speed referred to the vehicle speed during a
tip-in test at 27 km/h, with a 80%/20% front/rear wheel torque distribution; front
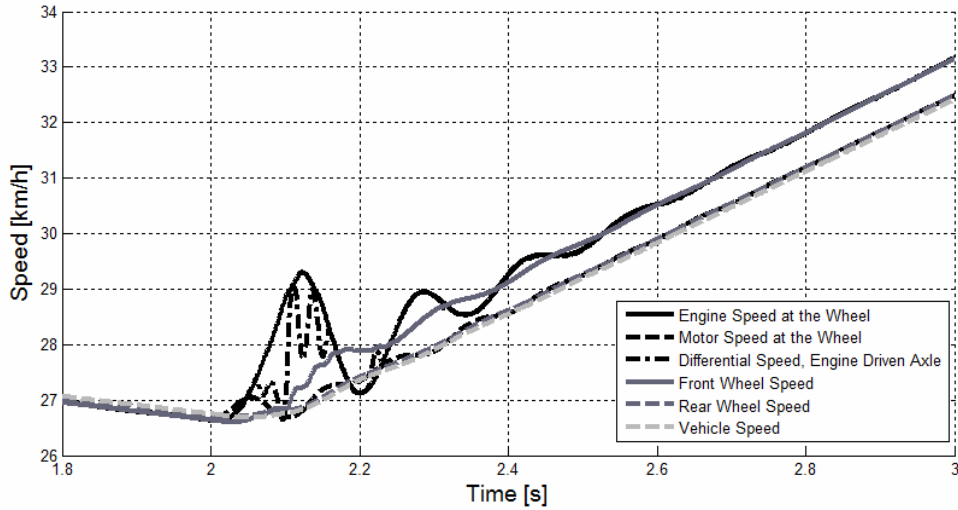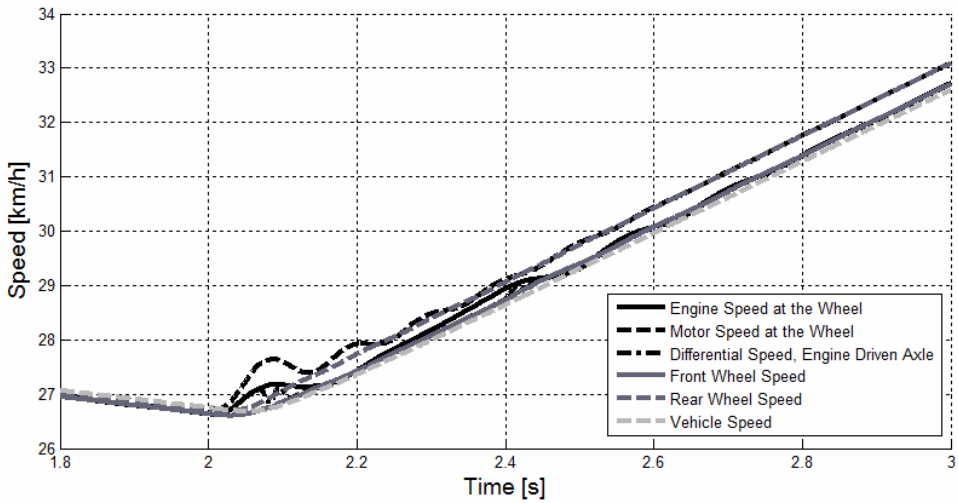transmission: third gear, rear transmission: second gear

Figure 12   Speed comparison with each component speed referred to the vehicle speed during a
tip-in test at 27 km/h, with a 20%/80% front/rear wheel torque distribution;
transmission: third gear, rear transmission: second gear

4.2   Principles of the anti-jerk control for the TTRP HEV

The results of the two powertrains in Section 3 and of the TTRP HEV in Section 4.1 demonstrate the need for an anti-jerk controller, which is required to damp the oscillations and make vehicle response consistent for the different combinations of wheel torque demands and gear ratios on the two axles. A first example of model-based anti-jerk control system was designed and implemented in the TTRP HEV model to

improve the vehicle response during abrupt torque demands, in conditions of constant gear ratio. A schematic of the anti-jerk control system is shown in Figure 13. The system only modifies the electric motor torque demand as the high level of torque controllability of the electric axle and the typically fast rise time result in a more effective anti-jerk control system than one based on the control of the ICE. The ICE keeps the empirical anti-jerk controller (not detailed here) of the original engine control unit (based on the operating parameters of the ICE), whilst the electric axle implements the supervisory anti-jerk control function.

Figure 13 Simplified schematic of the anti-jerk control system
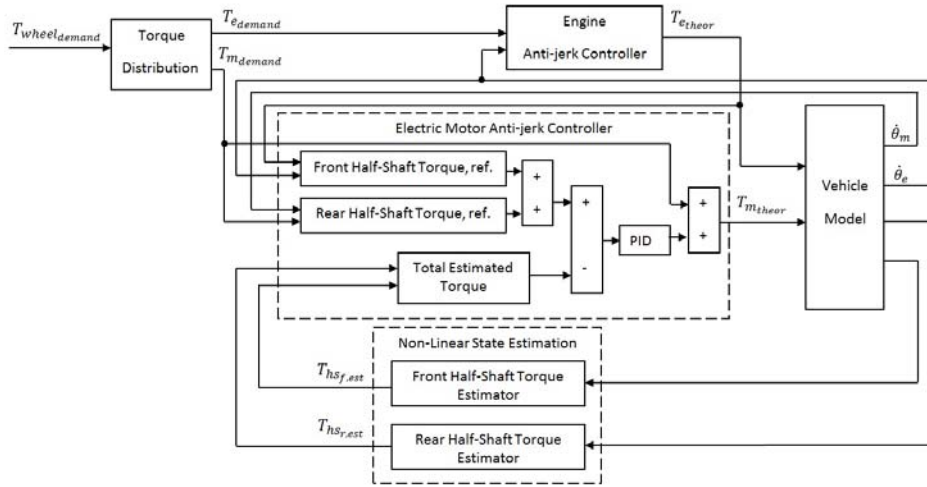
Two extended Kalman filters, based on the simplified models of the electric axle and the ICE drivetrain, estimate the half-shaft torque on each axle, as demonstrated in Amann et al. (2004), and Bottiglione et al. (2012) (the proposed filter has been adopted for this activity). The vehicle supervisory controller distributes the driver torque demand to the front and rear axles depending on a bias based on the operating conditions of the vehicle (powertrain temperatures, battery state of charge, etc.). The TTRP HEV controller proposed in this article calculates the overall reference half-shaft torque for the combined front and rear axle, starting from the driver torque demand, the engine speed and the electric motor speed, through the torque characteristics of the two propulsion units. The total reference and estimated half-shaft torques are then compared and the difference is the input into a proportional, integral, derivative (*PID*) controller to modify the electric motor torque demand. The demand is modified to eliminate the typical oscillations caused by the torsional dynamics, reported in Figures 11 and 12, which usually affect the vehicle acceleration response during tip-in tests.

Figure 14 shows examples of the Bode plots for the open-loop and closed-loop transfer functions (*OLTF* and *CLTF* respectively) for the electric motor *PID* and the vehicle system. The formulations for the open-loop and closed-loop transfer functions are given in equations (4.1) and (4.2). The frequency response of the front and rear half-shaft torques has been obtained through linearisation of the equations of the system, reported in Section 2, which have been implemented in a state-space formulation. Within equations (4.1) and (4.2) and Figure 14, the transfer functions resulting from the linearisation of the

extended Kalman filters have been neglected due to their fast dynamics. The conventional rules for tuning the *PID* feedback control system can be applied in order to achieve the desired tracking bandwidth.

$$OLTF = G_{PID}(s)\left(\frac{\overline{T}_{hs_f}}{\overline{T}_{m_{demand}}}(s) + \frac{\overline{T}_{hs_r}}{\overline{T}_{m_{demand}}}(s)\right) \tag{4.1}$$

$$CLTF = \frac{G_{PID}(s)\left(\dfrac{\overline{T}_{hs_f}}{\overline{T}_{m_{demand}}}(s) + \dfrac{\overline{T}_{hs_r}}{\overline{T}_{m_{demand}}}(s)\right)}{1 + G_{PID}(s)\left(\dfrac{\overline{T}_{hs_f}}{\overline{T}_{m_{demand}}}(s) + \dfrac{\overline{T}_{hs_r}}{\overline{T}_{m_{demand}}}(s)\right)} \tag{4.2}$$

Figure 14 Examples of Bode diagrams of the open-loop and closed-loop transfer functions for the feedback part of the electric motor based anti-jerk controller, for increasing values of the proportional gain *P* (indicated by the direction of the arrow in the figure) of the anti-jerk controller, for a condition of linearisation of the system
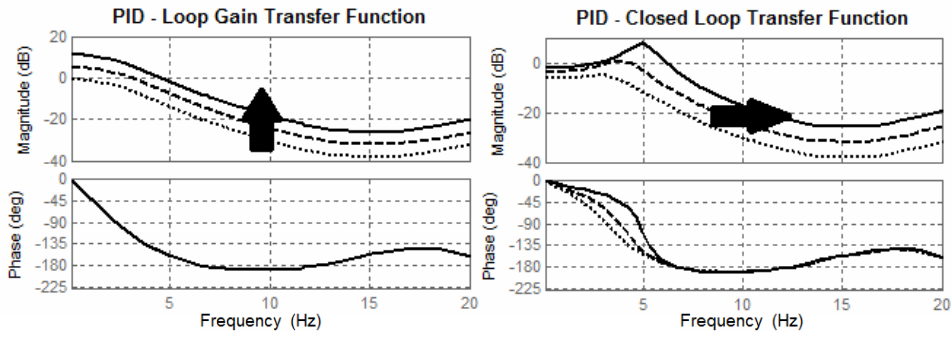

Particular care must be taken when selecting the gains of the controller, in order to prevent frequent saturations of the electric motor drive and their effect on the integral part of the *PID* controller. In this respect, an anti-wind up layout will have to be evaluated in a future upgrade to the *PID* controller.

To determine the effectiveness of the motor *PID* controller the frequency response of the system considering the vehicle acceleration was analysed. The transfer function providing the vehicle acceleration, $\overline{\overline{x}}$, for a requested combination of engine and electric motor demands is given below:

$$\overline{\overline{x}}(s) = T_{e_{demand}}\frac{\overline{\overline{x}}}{\overline{T}_{e_{demand}}}(s) +$$

$$+ \frac{\overline{\overline{x}}}{\overline{T}_{e_{demand}}}(s)\frac{\left(\begin{array}{l}G_{PID}(s)\left(T_{e_{demand}}i_{diff_f}i_{g_f} + T_{m_{demand}}i_{diff_r}i_{g_r}\right) - \\[6pt] T_{e_{demand}}G_{PID}(s)\left(\dfrac{\overline{T}_{hs_f}}{\overline{T}_{e_{demand}}}(s) + \dfrac{\overline{T}_{hs_r}}{\overline{T}_{e_{demand}}}(s)\right) + T_{m_{demand}}\end{array}\right)}{1 + G_{PID}(s)\dfrac{\overline{T}_{hs_f}}{\overline{T}_{m_{demand}}}(s) + G_{PID}(s)\dfrac{\overline{T}_{hs_r}}{\overline{T}_{m_{demand}}}(s)} \tag{4.3}$$

For example, Figure 15 illustrates the overall frequency response of the vehicle acceleration with a basic proportional controller included, compared with the frequency response of the TTRP HEV with no *PID* anti-jerk controller, except the standard anti-jerk controller of the engine. It is supposed that the two inputs (torque demands) to the system are phase synchronous. A sensitivity analysis of the effect of the value of the proportional gain (*P*) of the controller on the vehicle acceleration is carried out, where the proportional controller assumes the values P*, P*/2 and P*/4. The figure shows that a benefit in vehicle responsiveness is achieved by implementing an anti-jerk controller on the electric motor, due to the theoretically flat frequency response when the anti-jerk controller has a proportional gain value of P*/4. This ideal behaviour is not realistic when considering the torque saturation of the electric motor, which prevents achievement of the same response; however the frequency response characteristic provides a good insight into controller gain design. The transfer functions are heavily affected by the time constant τ_m of the electric motor air-gap torque dynamics (sometimes filtered at the power electronics control level for anti-jerk purposes) and in general by the selected linearisation point. In Figure 15, the response without the proportional controller is overdamped due to the test taking place at high speed, however at different linearisation points significantly underdamped behaviour can be seen.

Figure 15 Example of frequency response of the system with and without the PID including a sensitivity analysis of the proportional gain, for a set of linearisation conditions
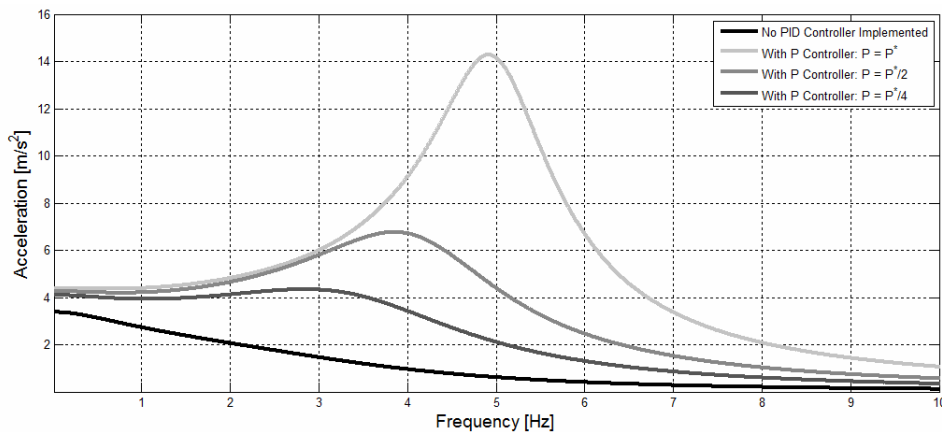
The acceleration profile for a tip-in test with the anti-jerk control system is compared with the same manoeuvre without the anti-jerk control system in Figure 16. The gains adopted on the *PID* controller are relatively high, however the model considers the torque saturation of the motor drive and the benefits of the controller are evident. Proper gain scheduling will be required for a consistent application of this controller to any driving condition. The anti-jerk control system can be seen to significantly reduce the oscillations in the acceleration profile, increasing driver comfort.

Figure 16 Acceleration profile comparison with and without the anti-jerk control system during a tip-in test at 27 km/h, with a 50%/50% front/rear percentage torque distribution (front transmission: third gear, rear transmission: first gear)
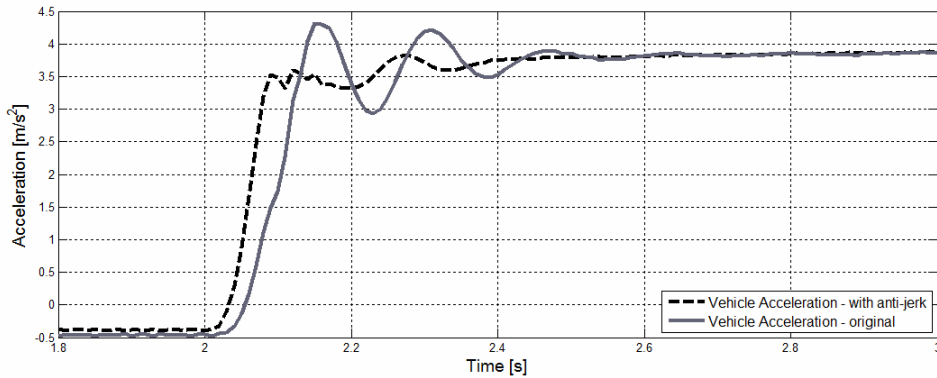
5   Conclusions and future work

A comprehensive non-linear model of the longitudinal dynamics of a TTRP HEV has been developed and presented. Each drivetrain model was validated against real world test data in a wide range of tip-in manoeuvres, proving the accuracy of the modelling methodology. A sensitivity analysis was then carried out through the variation of the torque distribution and gear ratios of the front and rear axles. A novel and significant contribution of the work has been the sensitivity analysis which showed a major modification of vehicle acceleration and jerk dynamics induced by the variation of the torque distribution between the front and rear axles, for the same steady-state value of vehicle longitudinal acceleration. This could provoke a sense of inconsistent drivability and discomfort in the driver and the passengers. Moreover, the electric axle can induce larger driveline oscillations due to the potentially very low rise time of the electric motor drive, which is further aggravated by the lack of a clutch damper. A novel anti-jerk control system has been successfully proposed and implemented to improve the overall vehicle acceleration profile through the modification of the electric motor torque demand.

The next step to be taken in this research will be to fully develop and validate the anti-jerk controller through the implementation of the required gain scheduling necessary for effectiveness in any operating condition, and through extensive testing against real-world data. Secondly, further development of the anti-jerk control system to be active during gearshifts is required to create a robust and comprehensive controller.

References

Amann, N., Böcker, J. and Prenner, F. (2004) 'Active damping of drivetrain oscillations for an electrically driven vehicle', *IEEE/ASME Transactions on Mechatronics*, Vol. 9, No. 4, pp.697–700.

Arata, J., Leamy, M.J., Meisel, J., Cunefare, K. and Taylor D. (2011) 'Backward-looking simulation of the Toyota Prius and General Motors two-mode power-split HEV powertrains', *SAE 2011 World Congress & Exhibition*, April, Detroit, USA, SAE 2011-01-0948.

Baumann, J., Kiencke, U., Swarnakar, A. and Schlegl, T.H. (2005) 'A robust design for anti-jerking', *SAE 2005 World Congress & Exhibition*, April, Detroit, USA, SAE 2005-01-0041.

Bottiglione, F., Sorniotti, A. and Shead, L. (2012) 'The effect of half-shaft torsion dynamics on the performance of a traction control system for electric vehicle', *IMechE Part D: Journal of Automobile Engineering*, Vol. 229, No. 9, pp.1145–1159.

Cavallino, C. (2009) 'Trasmissione a Due Marce Per Veicoli Elettrici', Oerlikon Graziano SpA, Italian Patent TO2009A000750.

Dorey, R.E. and Holmes, C.B. (1999) 'Vehicle drivability – its characterisation and measurement', *SAE World Congress and Exhibition*, March, Detroit, USA, SAE 1999-01-0949.

Eller, B. and Hetet, J.F. (2010) 'Study of an optimization criterion of mounting blocks for drivability evaluation of an EV', *VPPC Conference*, September, Lille, France, TR-3-2-4.

Fredriksson, J. (2006) 'Hybrid drivability of a hybrid vehicle using powertrain control', *International Journal of Alternative Propulsion*, Vol. 1, No. 1, pp.97–111.

Gupta, A.K., Landge, B.A. and Seth, B. (2009) 'Development of a parallel hybrid electric vehicle', SAE 2009-28-0045.

Huang, Q. and Wang, H. (2004) 'Fundamental study of jerk: evaluation of shift quality and ride comfort', *SAE 2004 Automotive Dynamics, Stability & Controls Conference and Exhibition*, May, Detroit, USA, SAE 2004-01-2065.

Kim, S., Park, J., Hong, J., Lee, M. and Sim, H. (2009) 'Transient control strategy of hybrid electric vehicle during mode change', *SAE World Congress and Exhibition*, April, Detroit, USA, SAE 2009-01-0228.

Morina, D. (2010) *Drivability Analysis of Four-Wheel-Drive Hybrid Vehicles*, MSc thesis, Politecnico Torino and University of Surrey.

Nise, N.S. (2004) *Control Systems Engineering*, 4th ed., John Wiley & Sons, Inc., New York, USA.

Pacejka, H.B. (2006) *Tyre and Vehicle Dynamics*, 2nd ed., Elsevier, Amsterdam, Netherlands.

Reimpell, J., Stoll, H. and Betzler, J.W. (2000) *The Automotive Chassis*, 2nd ed., Elsevier, Amsterdam, Netherlands.

Schöggl, P., Koegeler, H.M., Gschweitl, K., Kokal, H., Williams, P. and Hulak, K. (2001) 'Automated EMS calibration using objective drivability assessment and computer aided optimization methods', *SAE 2002 World Congress and Exhibition*, March, Detroit, USA, SAE 2002-01-0849.

Shin, S., Oh, J., Kim, J. and Hong, S. (2010) 'A method of gear-shift in parallel hybrid electric vehicle using motor control', *SAE World Congress and Exhibition*, April, Detroit, USA, SAE 2010-01-1305.

Shouren, Z. (1984) *Automatic Gearbox*, China Railway Press, Beijing.

Sorniotti, A. (2008) 'Driveline modeling, experimental validation and evaluation of the influence of the different parameters on the overall system dynamics', *SAE World Congress and Exhibition*, April, Detroit, USA, SAE 2008-01-0632.

Sorniotti, A., Loro Pilone, G., Viotto, F., Bertolotto, S., Barnes, R.J., Morrish, I., Everitt, M. (2011) 'A novel seamless 2-speed transmission system for electric vehicles: principles and simulation results', *SAE TO ZEV Conference*, Torino, Italy, June, SAE 2011-37-0022.

Torkzadeh, D., Baumann, J. and Kiencke, U. (2003) 'A neuro-fuzzy approach for anti-jerk control', *SAE World Congress and Exhibition*, March, Detroit, USA, SAE 2003-01-0361.

Appendix

List of the main vehicle parameters

	FWD ICE test vehicle	TTRP HEV
Vehicle mass [kg]	1,199	1,440
Weight distribution [%front/%rear]	61/39	50/50
Wheel base [m]	2.39	2.76
ICE – peak power [kW]	54	69
ICE – peak torque [Nm]	126	128
ICE trans. – 1st gear	3.909	3.47
ICE trans. – 2nd gear	2.158	2.514
ICE trans. – 3rd gear	1.480	1.822
ICE trans. – 4th gear	1.121	1.320
ICE trans. – 5th gear	0.897	0.956
ICE trans. – 6th gear	N/A	0.708
ICE trans. – diff. ratio	3.867	4
EM – peak power [kW]	N/A	70
EM – peak torque [Nm]	N/A	300
EM trans. – 1st gear	N/A	5.04
EM trans. – 2nd gear	N/A	2.61
EM trans. – diff. gear	N/A	2.24

List of notations – in order of appearance

Please note that the following subscripts were used within the text, with subscript '*r*' relating to 'rear', subscript '*f*' relating to 'front', subscript '*L*' relating to 'left', subscript '*R*' relating to 'right' and subscript '*est*' relating to 'estimated', subscripts 1 and 2 referring to 1st gear and 2nd gear respectively, unless specified differently. In the frequency domain, the parameters have the same notation as in the time domain, with a horizontal line above the symbol.

$\ddot{\theta}_w, \dot{\theta}_w, \theta_w$: wheel angular acceleration, speed and position

$\ddot{\theta}_e, \dot{\theta}_e$: angular acceleration and speed of ICE engine

$\ddot{\theta}_m, \dot{\theta}_m$: angular acceleration and speed of electric motor

$\ddot{\theta}_{diff}, \dot{\theta}_{diff}, \theta_{diff}$: differential angular acceleration, speed and position

$\ddot{\theta}_g, \dot{\theta}_g, \theta_g$: gearbox shaft angular acceleration, speed and position

i_{g1_r} : rear transmission first gear ratio

i_{g2_r} : rear transmission second gear ratio

i_{g_f} : front transmission gear ratio

η_{g1_r} : rear transmission first gear efficiency

η_{g2_r} : rear transmission second gear efficiency

η_{g_f} : front transmission gear efficiency

i_{diff}: differential ratio

η_{diff}: differential efficiency

J_{diff}: moment of inertia of the differential

β_{hs}: half-shaft torsional damping constant

K_{hs}: half-shaft torsional stiffness

β_d: clutch damper torsional damping constant

K_d: clutch damper torsional stiffness

$T_{e_{theor}}$: theoretical engine torque

$T_{e_{del}}$: delayed engine torque

T_{cd}: clutch damper torque

J_e: engine moment of inertia

T_{hs}: half-shaft torque

J_{hs}: half-shaft moment of inertia

η_{CVin}: constant velocity joint, inner, efficiency

$J_{trans_{ICE}}$: equivalent moment of inertia of the ICE powertrain

$J_{diff_{mech}}$: equivalent moment of inertia of the differential internals

$\Delta\ddot{\theta}_{diff}$: relative acceleration between the two sun gears of the differential

T_{roll}: rolling resistance torque

J_1: primary shaft moment of inertia

J_{1b}: clutch pack moment of inertia

J_2: secondary shaft moment of inertia

J_{2b}: sprag clutch pack moment of inertia

$T_{m_{del}}$: delayed electric motor torque

T_{fc}: friction clutch torque

J_{EM_1} : equivalent moment of inertia of the electric motor powertrain in first gear

J_{EM_2} : equivalent moment of inertia of the electric motor powertrain in second gear

m_{sm}: sprung mass

$\ddot{x}_{sm}, \dot{x}_{sm}, x_{sm}$: sprung mass longitudinal acceleration, speed and displacement

F_{j_x} : longitudinal force on the trailing arm joint

F_{j_z} : vertical force on the trailing arm joint

F_{aer}: aerodynamic drag force

$F_{RG,x_{sm}}$: sprung mass road grade force

c: horizontal distance between the front wheel centre and the front trailing arm joint

d: horizontal distance between the rear wheel centre and the rear trailing arm joint

e: vertical distance between the ground and the front trailing arm joint

f: vertical distance between the ground and the rear trailing arm joint

$T_{react.}$: reaction torque transmitted by the powertrain mounting system

$\ddot{z}_{sm}, \dot{z}_{sm}, z_{sm}$: sprung mass vertical acceleration, speed and displacement

$\Delta F_{RG,z_{sm}}$: variation(induced by the road grade) of the weight force component of the sprung mass perpendicular to the road surface

J_{sm}: sprung mass moment of inertia

$\ddot{\theta}_{sm}, \theta_{sm}$: sprung mass angular acceleration and displacement

L: vehicle wheelbase

a: front semi-wheelbase

b: rear semi-wheelbase

$H_{CG,sm}$: vertical distance between the centre of gravity of sprung mass and ground

G_{sm}: sprung mass centre of gravity

F_{s_z} : vertical suspension force

R_w: wheel radius

$F_{RG,us}$: unsprung mass force due to the road angle

ΔF_{us}: variation (induced by the road grade) of the weight force component of the unsprung mass perpendicular to the road surface

F_{t_x} : unsprung mass longitudinal tyre force

F_{t_z} : unsprung mass vertical tyre force

γ_f: unsprung mass trailing arm angle

m_{us}: unsprung mass

g: gravity

$\ddot{x}_{us}, x_{us}$: unsprung mass longitudinal acceleration and displacement

$\ddot{z}_{us}, z_{us}$: unsprung mass vertical acceleration and displacement

$T_{m_{theor}}$: theoretical electric motor torque

$T_{m_{demand}}$: electric motor torque demand

$T_{wheel_{demand}}$: wheel torque demand as a function of the driver input on the accelerator pedal

$T_{e_{demand}}$: ICE torque demand

G_{PID}: transfer function of the *PID* controller
s: Laplace variable